bioRxiv preprint doi: https://doi.org/10.1101/2020.10.17.343558; this version posted October 17, 2020. The copyright holder for this preprint (which was not certified by peer review) is the author/funder, who has granted bioRxiv a license to display the preprint in perpetuity. It is made available under aCC-BY-NC-ND 4.0 International license.

Distal CA1 maintains a more coherent spatial representation than proximal CA1 when local and global cues conflict

Sachin S. Deshmukh

Centre for Neuroscience,

Indian Institute of Science,

Bangalore

Correspondence

Sachin S. Deshmukh

Centre for Neuroscience,

Indian Institute of Science,

Bangalore

e-mail: sachin@iisc.ac.in

Pages: 30

Figures: 6

Tables: 4

Supplementary Figures: 1

Supplementary tables: 1

Running Title Functional segregation along the proximal distal axis of CA1

Acknowledgements

I thank Jeremy Johnson, Geeta Rao, Vyash Puliyadi, Amanda Smolinsky, Lou Blanpain, and Kimberley Christian for their support in data collection. This work was supported by Wellcome Trust/DBT India Alliance Grant IA/S/13/2/501024. Data collection was supported by R01 NS039456 (J. Knierim, PI).

Data Availability

The data that support the findings of this study are available from the corresponding author upon reasonable request.

Keywords: Hippocampus, Medial Entorhinal Cortex (MEC), Lateral Entorhinal Cortex (LEC),

bioRxiv preprint doi: https://doi.org/10.1101/2020.10.17.343558; this version posted October 17, 2020. The copyright holder for this preprint (which was not certified by peer review) is the author/funder, who has granted bioRxiv a license to display the preprint in perpetuity. It is made available under aCC-BY-NC-ND 4.0 International license.

Distal CA1 maintains a more coherent spatial representation than proximal CA1 when local and global cues conflict

Abstract

Entorhinal cortical projections show segregation along the transverse axis of CA1, with the medial entorhinal cortex (MEC) sending denser projections to proximal CA1 and the lateral entorhinal cortex (LEC) sending denser projections to distal CA1. Previous studies have reported functional segregation along the transverse axis of CA1 correlated with the functional differences in MEC and LEC. Proximal CA1 shows higher spatial selectivity than distal CA1 in these studies. We employ a double rotation paradigm, which creates an explicit conflict between local and global cues, to understand differential contributions of these reference frames to the spatial code in proximal and distal CA1. We show that proximal and distal CA1 respond differently to this local-global cue conflict. Proximal CA1 shows incoherent response consistent with the strong conflicting inputs it receives from MEC and distal CA3. In contrast, distal CA1 shows a more coherent rotation with global cues. In addition, our study fails to show the difference in spatial selectivity between proximal and distal CA1 seen in the previous studies, perhaps due to richer sensory information available in our behavior arena. Together these observations indicate that the functional segregation along proximodistal axis of CA1 is not merely of more or less spatial selectivity but that of the nature of the different inputs utilized to create and anchor spatial representations.

Introduction

The hippocampus is involved in spatial navigation and episodic memory (O'keefe and Nadel 1978; Squire et al. 2004). To understand the computations involved in these processes, it is critical to understand information transformation in the sub-regions of the entorhinal-hippocampal network. Cortical information to the hippocampus gets channeled through the medial and the lateral entorhinal cortex (MEC and LEC) (Burwell 2000; Witter and Amaral 2004). MEC and LEC are thought to convey complementary information to the hippocampus - path integration derived spatial information from MEC and sensory derived spatial and nonspatial information from LEC (Deshmukh and Knierim 2011; Hafting et al. 2005; Knierim et al. 2014; Manns and Eichenbaum 2009; Suzuki et al. 1997). While LEC and MEC layer II inputs to the dentate gyrus and CA3 are not segregated along the transverse axis of the hippocampus, layer III inputs to CA1 are. MEC projects preferentially to proximal CA1 (close to CA2), while LEC projects preferentially to distal CA1 (close to the subiculum) (Naber et al. 2001; Steward and

bioRxiv preprint doi: https://doi.org/10.1101/2020.10.17.343558; this version posted October 17, 2020. The copyright holder for this preprint (which was not certified by peer review) is the author/funder, who has granted bioRxiv a license to display the preprint in perpetuity. It is made available under aCC-BY-NC-ND 4.0 International license.

Scoville 1976; Witter and Amaral 2004). CA3 to CA1 projections also show segregation along the transverse axis, with proximal CA3 projecting preferentially to distal CA1 and distal CA3 projecting preferentially to proximal CA1 (Figure 1A) (Ishizuka et al. 1990; Witter and Amaral 2004).

As predicted by these anatomical differences, CA1 shows functional segregation along its transverse axis. In two-dimensional open fields and linear tracks, proximal CA1 is spatially more selective than distal CA1 (Henriksen et al. 2010; Ng et al. 2018; Oliva et al. 2016). Consistent with the predictions, distal CA1 neurons respond to objects and rewards (Burke et al. 2011; Xiao et al. 2020; these studies did not record from proximal CA1, so we do not know if there was a functional dissociation along the transverse axis). LEC and distal CA1 show enhanced oscillatory synchronization during olfactory-spatial associative memory, while LEC and proximal CA1 do not (Igarashi et al. 2014). Immediate early gene expression and lesion studies lend further support to spatial vs sensory double dissociation between proximal and distal CA1 (Ito and Schuman 2012; Nakamura et al. 2013; Nakazawa et al. 2016). However, the relative contributions of different inputs to the neural representations along the transverse axis of CA1 are not well understood.

A “double rotation” protocol (Knierim 2002; Shapiro et al. 1997) has been used extensively to study influence of local and global cues on spatial representations in different parts of the hippocampal formation. In this experimental protocol, prominent “local” on-track cues and “global” off-track cues are put in conflict by rotating them in the opposite directions. These experiments have revealed that CA1 responds to double rotation in an incoherent manner, while the CA3 rotates coherently with the local cues (Lee et al. 2004; Neunuebel and Knierim 2014). Along the transverse axis of CA3, proximal CA3 shows incoherent response while intermediate and distal CA3 shows coherent rotation with the local cues (Lee et al. 2015). In the same paradigm, MEC shows coherent rotation with the global cues. LEC, which shows very weak spatial tuning during the sessions with standard cue configuration, shows an extremely weak rotation with the local cues (Neunuebel et al. 2013). Thus, proximal CA1 gets strongly coherent but conflicting inputs from MEC (global) and distal CA3 (local), while distal CA1 gets incoherent inputs from proximal CA3 and weakly local inputs from LEC. The present study examines responses of CA1 neurons along the transverse axis to the double rotation manipulation to study how the entorhinal and CA3 input patterns affect CA1 representation along its transverse axis during local-global cue conflict.

Methods

bioRxiv preprint doi: https://doi.org/10.1101/2020.10.17.343558; this version posted October 17, 2020. The copyright holder for this preprint (which was not certified by peer review) is the author/funder, who has granted bioRxiv a license to display the preprint in perpetuity. It is made available under aCC-BY-NC-ND 4.0 International license.

Subjects and surgery

Eleven Long Evans rats aged 5-6 months were housed individually in 12:12 hour reversed day-night cycle. All experiments were performed during the night portion of the cycle. Animal care, surgical procedures and euthanasia procedures followed were in accordance with the National Institutes of Health guidelines and protocols approved by institutional animal care and use committee of the Johns Hopkins University. Custom built hyperdrives with independently moving 15 tetrodes and 2 references were implanted over the right hemisphere. Rats were implanted with 3D printed hyperdrives with linearly distributed bundle canulae angled at 35° to the ML axis to target the entire proximodistal extent of CA1 at the same septotemporal level. Data recorded during resting sessions from 8 of these rats was previously used for studying propagation of ripples in CA1 (Kumar and Deshmukh 2020).

Behavioral training and experimental protocol

Following recovery for about one week after surgery, rats were maintained at 80-90% of their free feeding weight in order to incentivize them to run on a circular track for food, during the training and the recording sessions. The circular track (56 cm inner diameter, 76 cm outer diameter) had 4 easily distinguishable sections, and was placed in a room with a 2.75 m diameter circular curtain with 6 large, distinct cues either hanging on the curtain or on the floor along the curtain (Knierim 2002). Once the rats learned to run in clockwise (CW) direction for food pellets randomly placed on the track, and the electrodes were deemed to be in optimal recording locations, the experimental sessions commenced. Each experimental day had 5-6 sessions of 15 laps each. The experimental sequence for one rat was STD-MIS-STD-MIS-STD, while that for all other rats was STD-STD-MIS-STD-MIS-STD. STD stands for standard configuration, and MIS stands for mismatch configuration with one out of the following mismatch angles selected in a pseudorandom order: 45°, 90°, 135°, and 180°. For a given mismatch angle, the local cues on the track were rotated counterclockwise (CCW) by half the amount and the global cues along the curtain were rotated CW by the other half. For example, the local cues were rotated by 22.5° CCW and the global cues were rotated by 22.5° CW for a 45° MIS session (Figure 1B). These manipulations were performed for 4 days, such that each mismatch angle was sampled twice.

Recording electronics

Neuronal data was collected using an analog wireless transmitter (Triangle Biosystems International, Durham, NC). Data from the wireless receiver was processed and stored using cheetah data acquisition system (Neuralynx Inc., Bozeman, MT). The signals were amplified 1000-10000 fold, bandpass filtered

bioRxiv preprint doi: https://doi.org/10.1101/2020.10.17.343558; this version posted October 17, 2020. The copyright holder for this preprint (which was not certified by peer review) is the author/funder, who has granted bioRxiv a license to display the preprint in perpetuity. It is made available under aCC-BY-NC-ND 4.0 International license.

between 600-6000 Hz, and digitized at 32000 Hz for single unit recordings. Any time one of the channels on a tetrode crossed a preset threshold, data from all 4 channels on the tetrode were recorded for 1ms (8 samples before and 24 samples after the threshold). Signals from one of the channels on each of the tetrodes were also amplified 500-2000 fold, bandpass filtered between 1-475 Hz, digitized at 1 KHz and stored continuously for local field potential (LFP) recordings.

Data analysis

Unit isolation

Single units were isolated using WinClust, a custom manual cluster cutting software (J. J. Knierim, Johns Hopkins University). For every threshold crossing, waveform characteristics such as peak, valley and energy on all 4 channels on a tetrode were used for clustering spikes. Only units with fair or better isolation as estimated by cluster separation, waveform and clean inter-spike interval histogram were included in subsequent analysis. Putative interneurons firing at ≥ 10 Hz mean firing rate were excluded.

Firing rate maps

Rat's position as well as heading direction was tracked using colored LEDs and a camera recording at 30 frames per second. Off track firing and intervals during which the rats ran slower than 2 cm/s or ran in the wrong direction (CCW) were excluded from the analysis in order to minimize firing rate variability introduced by non-spatial activity. Linearized rate maps were created at 1° resolution (which gives 360 bins for the circular track) by dividing the number of spikes when the rat was in each bin by the amount of time the rat spent in each bin. Linearized rate maps were smoothed using adaptive binning for computing spatial information scores (bits/spike; Skaggs et al. 1996) and gaussian filtered ($\sigma = 3°$) for other quantitative analyses. A shuffling procedure was used to determine the probability of obtaining the observed spatial information score by chance. Neuronal spike train was shifted by a random lag (minimum 30 s) with respect to the trajectory of the rat. Spatial information score was computed from adaptive binned, linearized rate map created from this shifted spike train. This procedure was repeated 1000 times to estimate the chance distribution of spatial information scores, and determine the number of randomly time shifted trials having spatial information scores greater than or equal to the observed spatial information scores. Only putative place cells that fired ≥ 20 spikes, and had statistically significant ($p < 0.01$) spatial information scores of ≥ 0.5 bits/spike in at least one of the MIS and preceding STD session were used in population vector correlation analysis and single unit responses.

bioRxiv preprint doi: https://doi.org/10.1101/2020.10.17.343558; this version posted October 17, 2020. The copyright holder for this preprint (which was not certified by peer review) is the author/funder, who has granted bioRxiv a license to display the preprint in perpetuity. It is made available under aCC-BY-NC-ND 4.0 International license.

Classification of single unit responses

Angle of rotation giving the highest Pearson correlation between STD and MIS was used as an estimate of rotation of the neuron. We categorized responses of putative place cells as "appear" (<20 spikes in STD but > 20 spikes in MIS), "disappear" (< 20 spikes in MIS but > 20 spikes in STD), "local" (highest Pearson correlation between STD and MIS after CCW rotation), "global" (highest Pearson correlation between STD and MIS after CW rotation), or "ambiguous" (Pearson correlation coefficient between STD and MIS not crossing a threshold of 0.6 after rotation, or the neuron not meeting the spatial information criteria in one of the sessions).

Population vector correlation analysis

Linearized rate maps were normalized by their peak firing rate before being used for constructing population vector. Normalized firing rates of all cells for each 1° bin in each MIS or STD session constituted the population vector for that bin for that session. STD vs MIS population vector correlation matrices were constructed by computing Pearson correlation coefficients of the 360 population vectors of each STD and MIS session with each other at all possible relative displacements (0-359°). Similarly, STD vs STD population vector correlation matrices were constructed from STD sessions before and after MIS (Lee et al. 2004). Mean population vector correlation at each relative displacement (0-359°) was computed from each population vector correlation matrix. Peaks (polar (length, angle) pairs converted to cartesian (x, y) pairs), as well as full width at half maximum (FWHM) were estimated from the mean population vector correlation. Normalized bias was defined as the difference between the mean population vector correlations for all displacements in the direction of local cue rotation (1-179°) and mean population vector correlations for all displacements in the direction of global cue rotation (181-359°) normalized by the mean population vector correlation for all displacements (0-359°). We performed bootstrap analysis by random sampling with replacement of neurons in the dataset to generate 1000 resampled datasets with the number of samples matching the number of samples in the actual dataset. Peaks of mean population vector correlations (x,y), FWHM, and normalized bias were calculated for each of the bootstrap iterations. Because these different parameters have different units and different magnitudes, they were normalized by subtracting their minima and dividing by the difference between their maxima and their minima. This led to all parameters having a range of 0 to 1. K-means clustering was used to partition the bootstrap distributions from proximal and distal CA1 into 2 clusters. Principal component analysis (PCA) was used to reduce dimensionality for display purpose.

bioRxiv preprint doi: https://doi.org/10.1101/2020.10.17.343558; this version posted October 17, 2020. The copyright holder for this preprint (which was not certified by peer review) is the author/funder, who has granted bioRxiv a license to display the preprint in perpetuity. It is made available under aCC-BY-NC-ND 4.0 International license.

Statistical analysis

MATLAB (Mathworks, Natick, MA) was used to perform statistical analysis. Circular statistics toolbox was used for statistical analysis of circular data. Units were tracked through a recording day, which typically had two MIS sessions with different mismatch angles. Tetrodes with multiple units were left undisturbed from one day to another, while those without units were moved ~16-32 µm in an attempt to increase the yield. For tetrodes with units on multiple days, no attempt was made to track units from one recording day to another. Therefore, while a number of units could be shared between sessions with different mismatch angles, we do not know the exact number of shared units. This partial overlap in number of units violates the assumption of independence made while correcting for multiple comparisons, such as Bonferroni or Holm-Bonferroni correction(Holm, 1979). Thus, rather than using corrections for multiple comparisons, patterns of low p values ($p < 0.05$) across multiple tests were used to draw conclusions. No conclusions were drawn based on single comparisons where multiple comparisons were performed simultaneously.

Histology

On the final day of recording, locations of a small subset of tetrodes was marked by passing 10 µA current for 10 s. Tetrode tracks were reconstructed from coronal sections and confirmed using marker lesion (Figure 1C; Deshmukh et al. 2010).

Results

Hyperdrives with 15 tetrodes and 2 references targeting the entire proximodistal extent of dorsal CA1 were implanted on 11 rats to record the activity of putative pyramidal cells as the rats ran CW on a circular track with 4 distinct textures (local cues) in a circular curtained room with 6 large global cues along the curtain. Cue manipulation sessions with global cues moving CW and local cues moving CCW by equal amounts creating 45°, 90°, 135°, or 180° mismatch (MIS) between the two were interleaved with sessions with cues in their standard configuration (STD) (Figure 1B).

Putative interneurons with mean firing rates > 10 Hz (Deshmukh and Knierim 2013; Fox and Ranck 1981; Frank et al. 2001; Ranck 1973) were excluded from analyses. Based on their locations, tetrodes were assigned to equally broad proximal, intermediate, and distal CA1 bands (Henriksen et al. 2010). Nine rats had putative pyramidal neurons recorded from in each of the three bands; one rat had units recorded from proximal and intermediate CA1; one rat had units recorded from proximal and distal CA1. Since

bioRxiv preprint doi: https://doi.org/10.1101/2020.10.17.343558; this version posted October 17, 2020. The copyright holder for this preprint (which was not certified by peer review) is the author/funder, who has granted bioRxiv a license to display the preprint in perpetuity. It is made available under aCC-BY-NC-ND 4.0 International license.

intermediate CA1 is expected to have overlapping entorhinal projections (Naber et al. 2001; Steward and Scoville 1976), although data from all three regions is displayed, quantitative statistical comparisons between regions were limited to proximal and distal CA1 by prior design.

Properties of single units along the proximodistal axis of CA1

In the first STD session, 156 well isolated putative pyramidal cells in proximal CA1 fired at least 20 spikes while the rat was running on the track; 131 neurons in intermediate CA1 and 180 neurons in distal CA1 met the same criteria. Mean and peak firing rates in proximal and distal CA1 were statistically indistinguishable from each other. Spatial correlates of neural activity were estimated using a variety of measures. Spatial information scores (bits/spike; Skaggs et al. 1996) in proximal and distal CA1 neurons were statistically indistinguishable from one another. Number of place fields/cell of 139 proximal and 140 distal CA1 place cells with statistically significant spatial information scores > 0.5 bits/spike were similarly indistinguishable, and so were the fraction of place cells with a single place field. Furthermore, sizes of 181 proximal and 176 distal CA1 place fields were statistically indistinguishable, and so was the fraction of track occupied by all the place fields of proximal and distal CA1 place cells (Figure 2, Table 1). This lack of difference in spatial correlates of proximal and distal CA1 persisted in MIS sessions irrespective of MIS angle. Spatial correlates showed a general decline from STD to MIS session in both regions (Supplementary Figure 1, Supplementary Table 1).

Single unit responses to cue manipulation

Responses to cue manipulation of putative place cells (≥ 20 spikes and spatial information score > 0.5 bits/spike in at least one of the STD or MIS session) were grouped into 5 classes as described previously from animals performing the same behavioral task (Lee et al. 2004; Neunuebel et al. 2013). Units that remained spatially selective in both STD and MIS sessions and showed maximum Pearson correlation after rotating the rate maps > 0.6 were classified as rotating neurons – those rotating CW were classified as rotating with global cues, while those rotating CCW were classified as rotating with local cues. Units that dropped below the 20 spikes threshold in MIS session were classified as disappearing units, while those that started firing more than 20 spikes in MIS after firing less than that in STD were classified as appearing units. Units that failed to meet the maximum Pearson correlation coefficient criterion as well as those which failed the spatial information score criteria in at least one of the sessions while firing more than 20 spikes in both sessions were classified as being ambiguous (Figure 3A). After pooling across all mismatch angles, proportions of appearing, disappearing, and ambiguous units were similar in

bioRxiv preprint doi: https://doi.org/10.1101/2020.10.17.343558; this version posted October 17, 2020. The copyright holder for this preprint (which was not certified by peer review) is the author/funder, who has granted bioRxiv a license to display the preprint in perpetuity. It is made available under aCC-BY-NC-ND 4.0 International license.

proximal and distal CA1, but proximal CA1 showed more units with CCW rotations in the direction of local cues while distal CA1 showed more units with CW rotations in the direction of global cues (Figure 3B). Many neurons are likely to have been recorded in more than one mismatch angles. In addition, classification of neurons into response classes creates arbitrary distinctions. For these two reasons, we did not perform quantitative statistical analysis on the distributions of neurons in these classes. Nonetheless, this classification provides a useful qualitative description of single unit responses that underlie the quantitative differences in populations of neurons across the transverse axis of CA1 discussed below.

Rotating cells showed clustering of rotation angles near the rotation angles of local or global cues in MIS sessions (Figure 4). These rotation angles were not distributed uniformly in 0-360° range for any of the mismatch angles for any of the CA1 subregions (Rao's spacing test, Table 2), confirming that they were not distributed by a random process with uniform distribution. Coherence of rotation of the rotating cells was estimated using mean vectors (Rayleigh test, Table 3). Proximal CA1 single units showed statistically significant coherent rotations at all mismatch angles. While the mean vectors (blue arrows in figure 4A) were rotated CCW towards local cues for 90°, 135° and 180°, the mean vector for 45° was rotated CW towards global cues. In contrast, mean vectors of distal CA1 single units showed CW rotations towards global cues for all mismatch angles. The mean vectors were statistically significant for all mismatch angles except 180°. There was no discernible pattern in the angles of rotation of mean vectors of single units in intermediate CA1, and the mean vectors were statistically significant only at 45°and 90°. Across all mismatch angles, proximal CA1 showed similar proportion of units rotating CW towards global cues (47%) and CCW towards local cues (53%). In contrast, both distal and intermediate CA1 showed a preference for CW rotation towards global cues (60% vs 40% CCW) (Figure 4B).

Population responses to cue manipulation

While the rotating single units in proximal and distal CA1 demonstrate clear differences, single unit rotation analysis misses out on contributions of other neurons in the ensemble excluded by the criteria used for classifying single unit responses to cue manipulations as rotating. Population vector correlations (Lee et al. 2015, Lee et al. 2004; Neunuebel et al. 2013) between sessions using all neurons meeting inclusion criteria (statistically significant spatial information scores > = 0.5 bits/spike, minimum 20 spikes, mean firing rate < 10 Hz) in either MIS or preceding STD session help overcome this limitation. Population vector correlations between STD sessions preceding and following MIS sessions (labelled STD1 and STD2) were used as control.

bioRxiv preprint doi: https://doi.org/10.1101/2020.10.17.343558; this version posted October 17, 2020. The copyright holder for this preprint (which was not certified by peer review) is the author/funder, who has granted bioRxiv a license to display the preprint in perpetuity. It is made available under aCC-BY-NC-ND 4.0 International license.

Figure 5 shows population vector correlations for STD1 vs STD2 and STD1 vs MIS for all MIS angles for proximal, intermediate, and distal CA1. Strength of correlation between the population vectors as estimated by Pearson correlation coefficients at all combinations of relative displacements is represented in pseudocolor, with black corresponding to <= 0 and white corresponding to 1. If the population representation is unchanged between the two sessions being compared (STD1 vs STD2 or STD1 vs MIS), the population vectors are expected to show highest correlation at 0° displacement from one another. This generates a line of highest correlation at the diagonal going from bottom left to top right of the population vector correlation matrix (black line). If, on the other hand the population representation coherently rotates between the two sessions being compared, the line of highest correlation (running at 45° angle, parallel to the diagonal) in the population vector correlation matrix is expected to get displaced by corresponding angle. Colored lines in each population vector correlation matrix show the expected displacement for the given MIS angle for local (red) and global (green) rotation. STD1 vs STD2 population vector correlation matrices for all MIS angles and CA1 subregions show a strong band of high correlation at the diagonal overlapping with the black line. This indicates that the population representations along the entire extent of CA1 transverse axis remained stable between STD sessions before and after the intervening MIS session regardless of the mismatch angle. In the 45° MIS session, all three regions showed strong population vector correlation bands, which were slightly displaced towards the green line corresponding to global cue rotation. In 90°, 135° and 180° MIS sessions, proximal CA1 did not show a single coherent band of high correlation parallel to the diagonal. Instead, patches of high correlations were seen overlapping with the local (red line) as well as global (green line) cue rotations. Intermediate CA1 showed a more coherent band of high correlation in 90° MIS session, which was biased towards the global cue rotation (green line) but showed a patchy distribution of high correlations similar to proximal CA1 in 135° and 180° MIS. In contrast to these two regions, distal CA1 showed a fairly coherent band of high correlation biased towards global cue rotation (green line) at all mismatch angles with occasional patches of high correlation near local cue rotations (red line).

To quantify the strength of the correlation bands, mean population vector correlation for each relative displacement (0°-359°) was calculated from 360 correlation bins along a line running parallel to the bottom left to top right diagonal. Displacement of the line from the diagonal corresponded to the relative displacement between the two sessions (STD1 vs STD2 or STD1 vs MIS). Mean population vector correlations (plotted on polar plots below each population vector correlation matrix in Figure 5) show a narrow distribution with large peaks at or near 0° displacement for STD1 vs STD2 comparisons for all

bioRxiv preprint doi: https://doi.org/10.1101/2020.10.17.343558; this version posted October 17, 2020. The copyright holder for this preprint (which was not certified by peer review) is the author/funder, who has granted bioRxiv a license to display the preprint in perpetuity. It is made available under aCC-BY-NC-ND 4.0 International license.

CA1 subregions, as expected when the representations remain stable between sessions being compared. Peaks in the polar plots of all STD1 vs MIS comparisons were smaller than the corresponding STD1 vs STD2 comparisons for all CA1 subregions. For STD1 vs MIS comparison for 45° mismatch angle, the distribution of mean population vector correlations widened and showed a bias towards CW rotations (in the direction of global cue rotation) in all CA1 subregions. As expected from the population vector correlation matrices, the polar plot for higher mismatch angles showed different patterns in different subregions of CA1. Proximal CA1 showed two comparable peaks of substantially reduced magnitude following local as well as global cue rotations in 90° and 135° MIS sessions, and a prominent but small peak rotating CCW (following local cue rotation) in 180° MIS session. Intermediate CA1 showed peaks rotating CW (following global cue rotation) in 90° and 180° MIS sessions, and a two peaked distribution in 135° MIS session. Distal CA1, in contrast to these two regions, showed consistent CW rotation with global cues in 90°, 135° and 180° MIS sessions, although very small peaks corresponding to local cue rotations could also be seen.

To compare proximal and distal CA1 population vector correlations explicitly, repeated sampling with replacement was performed 1000 times to generate bootstrapped distributions for the two regions. Number of samples in each iteration matched the number of samples in the real dataset for each subregion. For each of the iterations, population vector correlation matrices were generated and mean population vector correlation polar plots for each relative displacement were computed from those matrices. Following parameters were estimated from the polar plots to facilitate comparison between proximal and distal CA1: Peak vectors (x,y pairs), FWHM, and normalized bias (see methods for definitions of and calculations of these parameters). PCA was performed on this 4-dimensional space for reducing dimensionality for display purposes. Figure 6 shows the projection of the bootstrapped data for the two regions on the first two principal components for the different mismatch angles. Proximal CA1 bootstraps are shown in red while distal CA1 bootstraps are shown in blue. Three very clear patterns stand out in all four plots. First, the two distributions are well segregated along the two principal components, with the first principal component showing a clear segregation between the two at all mismatch angles other than 135°. Second, the distal CA1 bootstrap distribution is much more compact at all mismatch angles than the proximal CA1 bootstrap distribution. Third, the proximal CA1 bootstrap distribution often shows multiple clusters, while almost all distal CA1 boostraps stay together in a single compact cluster. In fact, the proximal CA1 bootstrap distribution for 135° mismatch shows 3 clusters with two clusters clearly segregated from the distal CA1 cluster and the third cluster overlapping with the distal CA1 cluster. All these patterns are consistent with the distal CA1 population maintaining more

bioRxiv preprint doi: https://doi.org/10.1101/2020.10.17.343558; this version posted October 17, 2020. The copyright holder for this preprint (which was not certified by peer review) is the author/funder, who has granted bioRxiv a license to display the preprint in perpetuity. It is made available under aCC-BY-NC-ND 4.0 International license.

a coherent representation across mismatch angles than the proximal CA1 population, in agreement with Figure 5.

To test whether these distributions of proximal and distal CA1 bootstraps are indeed different from one another in an unbiased manner, k-means clustering with k = 2 was employed. Figure 6 shows black and cyan circles for points classified into two clusters. Table 4 shows numbers of points from proximal and distal CA1 that were included in the two clusters. At 135° mismatch, all the distal CA1 points and a group of proximal CA1 points clustered together, while the remaining proximal CA1 points formed the other cluster. For all other mismatch angles, the clusters include more than 95% of the points from one region while including less than 5% of the points from the other region, as expected. These clustering patterns prove that proximal and distal CA1 respond differentially to the double rotation cue manipulation, and that distal CA1 population rotates more coherently than the proximal CA1 population.

Discussion

Spatial selectivity in proximal and distal CA1

In this study, putative pyramidal cells in proximal and distal CA1 show comparable spatial selectivity as estimated using spatial information score, number of place fields per cell, field size, and fraction of the track occupied by fields. This lack of difference in spatial selectivity along the transverse axis observed in STD as well as MIS sessions is in apparent conflict with higher spatial selectivity in proximal CA1 compared to distal CA1 in multiple earlier studies (Henriksen et al. 2010; Ng et al. 2018; Oliva et al. 2016). The behavioral arenas used in the earlier studies had single uniform texture, while the circular track in the present study had 4 easily discernible sections with distinct textures, visual appearances, and odors. Thus, the apparent elimination of differences in spatial selectivity between proximal and distal CA1 could possibly be caused by richer sensory information available from the behavioral arena. This observation adds a nuance to the established notion that distal CA1, which receives preferential projections from LEC (Naber et al. 2001; Steward and Scoville 1976; Witter and Amaral 2004), has lesser spatial selectivity.

LEC shows extremely weak spatial selectivity on the circular track used here, similar to that in a square box in simple and complex environments (Hargreaves et al. 2005; Neunuebel et al. 2013; Yoganarasimha et al. 2011). Hence, spatial selectivity of the inputs from LEC on the circular track is insufficient to explain higher spatial selectivity in distal CA1 in the present study. Plausible mechanisms for global cue control of distal CA1 during double rotation are discussed below. However, these projections from MEC

bioRxiv preprint doi: https://doi.org/10.1101/2020.10.17.343558; this version posted October 17, 2020. The copyright holder for this preprint (which was not certified by peer review) is the author/funder, who has granted bioRxiv a license to display the preprint in perpetuity. It is made available under aCC-BY-NC-ND 4.0 International license.

(Masurkar et al. 2017), nucleus reuniens (Dolleman-van der Weel et al. 2019; Dolleman-Van Der Weel and Witter 1996; Vertes et al. 2006), and the subiculum (Ding 2013; Xu et al. 2016) may not be sufficient on their own to explain why the spatial selectivity differences along the transverse axis of CA1 seen in the previous studies (Henriksen et al. 2010; Ng et al. 2018; Oliva et al. 2016) disappear in the present study in the presence of distinct sensory cues on track. Increased complexity of the environment and/or availability of the on-track sensory cues increasing spatial selectivity of existing non-LEC inputs or altering responsiveness of distal CA1 to these inputs are different mechanisms by which this can be achieved. Further studies are required to test if one or both of these mechanisms contribute to increased spatial selectivity in distal CA1, including the role of LEC as the possible modulator of contributions of non-LEC inputs to CA1 spatial code (Lu et al. 2013).

Dissociation of responses to double rotation manipulation between proximal and distal CA1

EC and CA3 inputs to proximal and distal CA1 respond very differently to double rotation, leading to an expectation that the responses to this manipulation will differ along the transverse axis of CA1. Proximal CA1 receives strong competing inputs from CA3 and MEC during MIS sessions. Distal CA3 rotates coherently with local cues (Lee et al. 2015), while MEC rotates coherently with global cues (Neunuebel et al. 2013). In contrast, distal CA1 does not receive a strong, coherently rotating signal from either CA3 or LEC. Proximal CA3 responds incoherently to double rotation, with sporadic hotspots of high correlation in the population vector correlation matrices of MIS angles larger than 45° rather than a band of high correlation following either the local or the global cues (Lee et al. 2015). The sporadic hotspots of high correlation are sometimes seen rotating with local cues while rotating with global cues at other times. LEC neurons show a very weak spatial selectivity on the circular track in STD sessions (Yoganarasimha et al. 2011). Neither the STD1 vs STD2 nor STD1 vs MIS population vector correlation matrices for LEC show a narrow band of high correlation, but polar plots of mean population vector correlations reveal a weak but statistically significant preference for rotating with local cues (Neunuebel et al. 2013). LEC encodes external items in egocentric coordinates (Wang et al. 2018), but in the present task, the allocentric and the egocentric reference frames are confounded, since the rat typically faces in a certain direction at each position on track. This translates into distances and directions to different cues being practically fixed at each position. Hence, we do not expect the response of the LEC neurons to double rotation manipulation to appear different between the two reference frames and expect the local cues to weakly dominate over global cues (Neunuebel et al. 2013) even in the egocentric reference frame.

bioRxiv preprint doi: https://doi.org/10.1101/2020.10.17.343558; this version posted October 17, 2020. The copyright holder for this preprint (which was not certified by peer review) is the author/funder, who has granted bioRxiv a license to display the preprint in perpetuity. It is made available under aCC-BY-NC-ND 4.0 International license.

These weakly local and incoherent inputs from LEC and proximal CA1 would predict either incoherent or weakly local response in distal CA1. Surprisingly, distal CA1 shows coherent rotation with global cues in this study. Alternative sources of spatial information anchored to global cues need to be considered to explain these results. One possibility is that in absence of strong competing inputs, even sparse projections from MEC (Masurkar et al. 2017) might be sufficient to cause distal CA1 neurons to rotate with global cues. In addition to EC inputs, CA1 receives other inputs which could potentially influence spatial representation in distal CA1 in this task. Nucleus reuniens, which connects to the medial prefrontal cortex and the hippocampus (Dolleman-van der Weel et al. 2019; Dolleman-Van Der Weel and Witter 1996; Vertes et al. 2006), sends direct projections to CA1 and shows head direction cells (Jankowski et al. 2014), place cells, and border cells (Jankowski et al. 2015). While nucleus reuniens neurons have not been recorded in the double rotation task, head direction cells recorded in other thalamic nuclei (ADN, AVN, LDN, VAN and RT) rotate with the global cues in the double rotation task (Yoganarasimha et al. 2006). Anecdotally, we as well as others (Peyrache and Buzsaki, https://www.youtube.com/watch?v=2da6gzF9eo0&t=24m13s) have recorded putative axons with head direction tuning outside pyramidal cell layer in distal CA1. Notwithstanding the source of these head direction projections, this anecdotal observation further supports the hypothesis that head direction inputs may be involved in coherent rotation of distal CA1 with global cues. Subiculum, which receives direct projections from the head direction system as well as MEC (Ding 2013), sends feedback projections to CA1 (Xu et al. 2016), and rotates coherently with global cues in the double rotation task (Sharma et al. 2020). While these inputs from MEC, nucleus reuniens, and the subiculum to distal CA1 may be less numerous than LEC and proximal CA3, they may be strong enough to drive distal CA1 to rotate with global cues in absence of competing strong inputs rotating with local cues.

In contrast to distal CA1, proximal CA1 gets strong, conflicting inputs from distal CA3 (Lee et al. 2015) and MEC (Neunuebel et al. 2013) rotating with local and global cues respectively during double rotation. CA1 is hypothesized to be a mismatch detector that compares recalled/predictive information from CA3 with the current status information from EC layer III (Duncan et al. 2009; Fyhn et al. 2002; Hasselmo et al. 1995; Hasselmo and Schnell 1994; Kumaran and Maguire 2006; Lisman and Grace 2005; Lörincz and Buzsáki 2000; Vinogradova 2001). Strong conflicting inputs from CA3 and MEC to proximal CA1 during double rotation create ideal conditions to test the performance of proximal CA1 as mismatch detector. If proximal CA1 performs as a mismatch detector during double rotation, it should show enhanced activity with coherent rotation with MEC input. Instead, proximal CA1 shows incoherent response to double rotation and lack of increased mean or peak firing rate in the MIS sessions (Supplementary Figure 1 and

bioRxiv preprint doi: https://doi.org/10.1101/2020.10.17.343558; this version posted October 17, 2020. The copyright holder for this preprint (which was not certified by peer review) is the author/funder, who has granted bioRxiv a license to display the preprint in perpetuity. It is made available under aCC-BY-NC-ND 4.0 International license.

Supplementary Table 1). The incoherent response of the present study may, instead, be explained by differential strengths of CA3 and MEC inputs to individual proximal CA1 neurons driving the variety of responses observed there. Neurons with predominant inputs from either CA3 or MEC may follow that input, while those without a clearly dominant input from CA3 and MEC may give ambiguous or remapping responses. These results, however, do not eliminate the possibility that the individual CA1 neurons that appear during MIS sessions act as mismatch detectors.

Spatial representation in CA1

Since the discovery of place cells (O'Keefe 1976; O'Keefe and Dostrovsky 1971), spatial representation in the hippocampus is thought to be a unitary representation of absolute space (O'keefe and Nadel 1978). This unitary representation requires a single reference frame with a single origin with respect to which every point of space is encoded. However, it is possible that the hippocampal spatial representation might appear to be unitary, without there being an explicitly unitary representation of space. A number of independent reference frames/spatial representations may coexist, and may generally agree with one another, giving an appearance of a unitary code for space. Thus, different neurons firing at a specific location may be encoding that location as different distances and directions from different origins. Some experimental conditions demonstrate existence of such coexisting reference frames in CA1. Representations of proximity to barriers (Rivard et al. 2004), goal location (Fyhn et al. 2002; Gothard et al. 1996b), distance and direction to goal (Gothard et al. 1996a; Sarel et al. 2017), distance and direction to landmarks (Deshmukh and Knierim 2013; McNaughton et al. 1995) may coexist with classic place cells representing space in allocentric coordinates. These place fields in allocentric coordinates themselves may be formed by combining inputs from two or more boundary vector cells (Hartley et al. 2000; O'Keefe and Burgess 1996) or grid cells (de Almeida et al. 2009; Monaco et al. 2011; Savelli and Knierim 2010; Solstad et al. 2006), or a combination of sensory and self-generated inputs (Deshmukh and Knierim 2013). Thus, they may be encoding space in different reference frames.

Creating an explicit conflict between reference frames reveals their influence on hippocampal representation of space (Gothard et al. 1996a, 1996b; Knierim 2002; Lee et al. 2004; Zinyuk et al. 2000). In the double rotation paradigm used in this paper, some regions involved in spatial encoding show coherent rotations while the others show weak to no coherence in rotation (Lee et al. 2015, 2004; Neunuebel et al. 2013; Neunuebel and Knierim 2014; Sharma et al. 2020). The dissociation of responses to double rotation manipulation along the proximodistal axis of CA1 shown here demonstrates that the non-unitary representation of space in the hippocampal output (via CA1) reflects strong conflict

bioRxiv preprint doi: https://doi.org/10.1101/2020.10.17.343558; this version posted October 17, 2020. The copyright holder for this preprint (which was not certified by peer review) is the author/funder, who has granted bioRxiv a license to display the preprint in perpetuity. It is made available under aCC-BY-NC-ND 4.0 International license.

apparent in its inputs (in proximal CA1) or lack thereof (in distal CA1). Regions of the brain differentially targeted (directly or indirectly) by proximal and distal CA1 (Naber et al. 2001; Witter and Amaral 2004), thus, receive spatial inputs that have differential influence of different spatial reference frames. Further studies are required to elaborate the role of this difference of spatial inputs in functioning of these target regions.

References

de Almeida L, **Idiart M**, **Lisman JE**. The input-output transformation of the hippocampal granule cells: from grid cells to place fields. *J Neurosci* 29: 7504–7512, 2009.

Burke SN, **Maurer AP**, **Nematollahi S**, **Uprety AR**, **Wallace JL**, **Barnes CA**. The influence of objects on place field expression and size in distal hippocampal CA1. *Hippocampus* 21: 783–801, 2011.

Burwell RD. The parahippocampal region: corticocortical connectivity. *Ann N Y Acad Sci* 911: 25–42, 2000.

Deshmukh SS, **Knierim JJ**. Representation of non-spatial and spatial information in the lateral entorhinal cortex. *Front Behav Neurosci* 5: 69, 2011.

Deshmukh SS, **Knierim JJ**. Influence of local objects on hippocampal representations: Landmark vectors and memory. *Hippocampus* 23: 253–267, 2013.

Deshmukh SS, **Yoganarasimha D**, **Voicu H**, **Knierim JJ**. Theta modulation in the medial and the lateral entorhinal cortices. *J Neurophysiol* 104: 994–1006, 2010.

Ding S-L. Comparative anatomy of the prosubiculum, subiculum, presubiculum, postsubiculum, and parasubiculum in human, monkey, and rodent. *J Comp Neurol* 521: 4145–4162, 2013.

Dolleman-van der Weel MJ, **Griffin AL**, **Ito HT**, **Shapiro ML**, **Witter MP**, **Vertes RP**, **Allen TA**. The nucleus reuniens of the thalamus sits at the nexus of a hippocampus and medial prefrontal cortex circuit enabling memory and behavior. *Learn Mem* 26: 191–205, 2019.

Dolleman-Van Der Weel MJ, **Witter MP**. Projections from the nucleus reuniens thalami to the entorhinal cortex, hippocampal field CA1, and the subiculum in the rat arise from different populations of neurons. *J Comp Neurol* 364: 637–650, 1996.

Duncan K, **Curtis C**, **Davachi L**. Distinct memory signatures in the hippocampus: intentional States distinguish match and mismatch enhancement signals. *J Neurosci* 29: 131–139, 2009.

Fox SE, **Ranck JB**. Electrophysiological characteristics of hippocampal complex-spike cells and theta cells. *Exp Brain Res* 41: 399–410, 1981.

Frank LM, **Brown EN**, **Wilson MA**. A comparison of the firing properties of putative excitatory and inhibitory neurons from CA1 and the entorhinal cortex. *J Neurophysiol* 86: 2029–2040, 2001.

bioRxiv preprint doi: https://doi.org/10.1101/2020.10.17.343558; this version posted October 17, 2020. The copyright holder for this preprint (which was not certified by peer review) is the author/funder, who has granted bioRxiv a license to display the preprint in perpetuity. It is made available under aCC-BY-NC-ND 4.0 International license.

Fyhn M, **Molden S**, **Hollup S**, **Moser M-B**, **Moser E**. Hippocampal neurons responding to first-time dislocation of a target object. *Neuron* 35: 555–566, 2002.

Gothard KM, **Skaggs WE**, **McNaughton BL**. Dynamics of mismatch correction in the hippocampal ensemble code for space: interaction between path integration and environmental cues. *J Neurosci* 16: 8027–8040, 1996a.

Gothard KM, **Skaggs WE**, **Moore KM**, **McNaughton BL**. Binding of hippocampal CA1 neural activity to multiple reference frames in a landmark-based navigation task. *J Neurosci* 16: 823–835, 1996b.

Hafting T, **Fyhn M**, **Molden S**, **Moser M-B**, **Moser EI**. Microstructure of a spatial map in the entorhinal cortex. *Nature* 436: 801–806, 2005.

Hargreaves EL, **Rao G**, **Lee I**, **Knierim JJ**. Major dissociation between medial and lateral entorhinal input to dorsal hippocampus. *Science* 308: 1792–1794, 2005.

Hartley T, **Burgess N**, **Lever C**, **Cacucci F**, **O'Keefe J**. Modeling place fields in terms of the cortical inputs to the hippocampus. *Hippocampus* 10: 369–379, 2000.

Hasselmo ME, **Schnell E**. Laminar selectivity of the cholinergic suppression of synaptic transmission in rat hippocampal region CA1: computational modeling and brain slice physiology. *J Neurosci* 14: 3898–3914, 1994.

Hasselmo ME, **Schnell E**, **Barkai E**. Dynamics of learning and recall at excitatory recurrent synapses and cholinergic modulation in rat hippocampal region CA3. *J Neurosci* 15: 5249–5262, 1995.

Henriksen EJ, **Colgin LL**, **Barnes CA**, **Witter MP**, **Moser M-B**, **Moser EI**. Spatial representation along the proximodistal axis of CA1. *Neuron* 68: 127–137, 2010.

Holm, Sture. A Simple Sequentially Rejective Multiple Test Procedure. *Scand J Stat* 6: 65–70, 1979.

Igarashi KM, **Lu L**, **Colgin LL**, **Moser M-B**, **Moser EI**. Coordination of entorhinal-hippocampal ensemble activity during associative learning. *Nature* 510: 143–147, 2014.

Ishizuka N, **Weber J**, **Amaral DG**. Organization of intrahippocampal projections originating from CA3 pyramidal cells in the rat. *J Comp Neurol* 295: 580–623, 1990.

Ito HT, **Schuman EM**. Functional division of hippocampal area CA1 via modulatory gating of entorhinal cortical inputs. *Hippocampus* 22: 372–387, 2012.

Jankowski MM, **Islam MN**, **Wright NF**, **Vann SD**, **Erichsen JT**, **Aggleton JP**, **O'Mara SM**. Nucleus reuniens of the thalamus contains head direction cells. *Elife* 3, 2014.

Jankowski MM, **Passecker J**, **Islam MN**, **Vann S**, **Erichsen JT**, **Aggleton JP**, **O'Mara SM**. Evidence for spatially-responsive neurons in the rostral thalamus. *Front Behav Neurosci* 9: 256, 2015.

Knierim JJ. Dynamic interactions between local surface cues, distal landmarks, and intrinsic circuitry in hippocampal place cells. *J Neurosci* 22: 6254–6264, 2002.

bioRxiv preprint doi: https://doi.org/10.1101/2020.10.17.343558; this version posted October 17, 2020. The copyright holder for this preprint (which was not certified by peer review) is the author/funder, who has granted bioRxiv a license to display the preprint in perpetuity. It is made available under aCC-BY-NC-ND 4.0 International license.

Knierim JJ, **Neunuebel JP**, **Deshmukh SS**. Functional correlates of the lateral and medial entorhinal cortex: objects, path integration and local-global reference frames. *Philos Trans R Soc Lond, B, Biol Sci* 369: 20130369, 2014.

Kumar M, **Deshmukh SS**. Differential propagation of ripples along the proximodistal and septotemporal axes of dorsal CA1 of rats. *Hippocampus* , 2020. doi:10.1002/hipo.23211.

Kumaran D, **Maguire EA**. An unexpected sequence of events: mismatch detection in the human hippocampus. *PLoS Biol* 4: e424, 2006.

Lee H, **Wang C**, **Deshmukh SS**, **Knierim JJ**. Neural Population Evidence of Functional Heterogeneity along the CA3 Transverse Axis: Pattern Completion versus Pattern Separation. *Neuron* 87: 1093–1105, 2015.

Lee I, **Yoganarasimha D**, **Rao G**, **Knierim JJ**. Comparison of population coherence of place cells in hippocampal subfields CA1 and CA3. *Nature* 430: 456–459, 2004.

Lisman JE, **Grace AA**. The hippocampal-VTA loop: controlling the entry of information into long-term memory. *Neuron* 46: 703–713, 2005.

Lörincz A, **Buzsáki G**. Two-phase computational model training long-term memories in the entorhinal-hippocampal region. *Ann N Y Acad Sci* 911: 83–111, 2000.

Lu L, **Leutgeb JK**, **Tsao A**, **Henriksen EJ**, **Leutgeb S**, **Barnes CA**, **Witter MP**, **Moser M-B**, **Moser EI**. Impaired hippocampal rate coding after lesions of the lateral entorhinal cortex. *Nat Neurosci* 16: 1085–1093, 2013.

Manns JR, **Eichenbaum H**. A cognitive map for object memory in the hippocampus. *Learn Mem* 16: 616–624, 2009.

Masurkar AV, **Srinivas KV**, **Brann DH**, **Warren R**, **Lowes DC**, **Siegelbaum SA**. Medial and Lateral Entorhinal Cortex Differentially Excite Deep versus Superficial CA1 Pyramidal Neurons. *Cell Rep* 18: 148–160, 2017.

McNaughton BL, **Knierim JJ**, **Wilson MA**. Vector encoding and the vestibular foundations of spatial cognition: Neurophysiological and computational mechanisms. In: *The Cognitive Neurosciences*. Cambridge, MA: MIT Press, 1995, p. 585–595.

Monaco JD, **Abbott LF**, **Abbott LF**. Modular realignment of entorhinal grid cell activity as a basis for hippocampal remapping. *The Journal of Neuroscience: The Official Journal of the Society for Neuroscience* 31: 9414–9425, 2011.

Naber PA, **Lopes da Silva FH**, **Witter MP**. Reciprocal connections between the entorhinal cortex and hippocampal fields CA1 and the subiculum are in register with the projections from CA1 to the subiculum. *Hippocampus* 11: 99–104, 2001.

Nakamura NH, **Flasbeck V**, **Maingret N**, **Kitsukawa T**, **Sauvage MM**. Proximodistal segregation of nonspatial information in CA3: preferential recruitment of a proximal CA3-distal CA1 network in nonspatial recognition memory. *J Neurosci* 33: 11506–11514, 2013.

bioRxiv preprint doi: https://doi.org/10.1101/2020.10.17.343558; this version posted October 17, 2020. The copyright holder for this preprint (which was not certified by peer review) is the author/funder, who has granted bioRxiv a license to display the preprint in perpetuity. It is made available under aCC-BY-NC-ND 4.0 International license.

Nakazawa Y, **Pevzner A**, **Tanaka KZ**, **Wiltgen BJ**. Memory retrieval along the proximodistal axis of CA1. *Hippocampus* 26: 1140–1148, 2016.

Neunuebel JP, **Knierim JJ**. CA3 retrieves coherent representations from degraded input: direct evidence for CA3 pattern completion and dentate gyrus pattern separation. *Neuron* 81: 416–427, 2014.

Neunuebel JP, **Yoganarasimha D**, **Rao G**, **Knierim JJ**. Conflicts between local and global spatial frameworks dissociate neural representations of the lateral and medial entorhinal cortex. *J Neurosci* 33: 9246–9258, 2013.

Ng C-W, **Elias GA**, **Asem JSA**, **Allen TA**, **Fortin NJ**. Nonspatial sequence coding varies along the CA1 transverse axis. *Behav Brain Res* 354: 39–47, 2018.

O'Keefe J. Place units in the hippocampus of the freely moving rat. *Exp Neurol* 51: 78–109, 1976.

O'Keefe J, **Burgess N**. Geometric determinants of the place fields of hippocampal neurons. *Nature* 381: 425–428, 1996.

O'Keefe J, **Dostrovsky J**. The hippocampus as a spatial map. Preliminary evidence from unit activity in the freely-moving rat. *Brain Res* 34: 171–175, 1971.

O'keefe J, **Nadel L**. *The hippocampus as a cognitive map*. Oxford: Clarendon Press, 1978.

Oliva A, **Fernández-Ruiz A**, **Buzsáki G**, **Berényi A**. Spatial coding and physiological properties of hippocampal neurons in the Cornu Ammonis subregions. *Hippocampus* 26: 1593–1607, 2016.

Ranck JB. Studies on single neurons in dorsal hippocampal formation and septum in unrestrained rats. I. Behavioral correlates and firing repertoires. *Exp Neurol* 41: 461–531, 1973.

Rivard B, **Li Y**, **Lenck-Santini P-P**, **Poucet B**, **Muller RU**. Representation of objects in space by two classes of hippocampal pyramidal cells. *J Gen Physiol* 124: 9–25, 2004.

Sarel A, **Finkelstein A**, **Las L**, **Ulanovsky N**. Vectorial representation of spatial goals in the hippocampus of bats. *Science* 355: 176–180, 2017.

Savelli F, **Knierim JJ**. Hebbian analysis of the transformation of medial entorhinal grid-cell inputs to hippocampal place fields. *Journal of Neurophysiology* 103: 3167–3183, 2010.

Shapiro ML, **Tanila H**, **Eichenbaum H**. Cues that hippocampal place cells encode: dynamic and hierarchical representation of local and distal stimuli. *Hippocampus* 7: 624–642, 1997.

Sharma A, **Nair IR**, **Doreswamy Y**. Attractor-like spatial representations in the Subicular Complex network. *bioRxiv* 2020.02.05.935379, 2020.

Skaggs WE, **McNaughton BL**, **Wilson MA**, **Barnes CA**. Theta phase precession in hippocampal neuronal populations and the compression of temporal sequences. *Hippocampus* 6: 149–172, 1996.

Solstad T, **Moser EI**, **Einevoll GT**. From grid cells to place cells: a mathematical model. *Hippocampus* 16: 1026–1031, 2006.

bioRxiv preprint doi: https://doi.org/10.1101/2020.10.17.343558; this version posted October 17, 2020. The copyright holder for this preprint (which was not certified by peer review) is the author/funder, who has granted bioRxiv a license to display the preprint in perpetuity. It is made available under aCC-BY-NC-ND 4.0 International license.

Steward O, **Scoville SA**. Cells of origin of entorhinal cortical afferents to the hippocampus and fascia dentata of the rat. *J Comp Neurol* 169: 347–370, 1976.

Suzuki WA, **Miller EK**, **Desimone R**. Object and Place Memory in the Macaque Entorhinal Cortex. *Journal of Neurophysiology* 78: 1062–1081, 1997.

Vertes RP, **Hoover WB**, **Do Valle AC**, **Sherman A**, **Rodriguez JJ**. Efferent projections of reuniens and rhomboid nuclei of the thalamus in the rat. *J Comp Neurol* 499: 768–796, 2006.

Vinogradova OS. Hippocampus as comparator: role of the two input and two output systems of the hippocampus in selection and registration of information. *Hippocampus* 11: 578–598, 2001.

Wang C, **Chen X**, **Lee H**, **Deshmukh SS**, **Yoganarasimha D**, **Savelli F**, **Knierim JJ**. Egocentric coding of external items in the lateral entorhinal cortex. *Science* 362: 945–949, 2018.

Witter MP, **Amaral DG**. In: *Hippocampal Formation*. Elsevier, p. 635–704.https://ucdavis.pure.elsevier.com/en/publications/hippocampal-formation [5 Aug. 2020].

Xiao Z, **Lin K**, **Fellous J-M**. Conjunctive reward-place coding properties of dorsal distal CA1 hippocampus cells. *Biol Cybern* 114: 285–301, 2020.

Xu X, **Sun Y**, **Holmes TC**, **López AJ**. Noncanonical connections between the subiculum and hippocampal CA1. *J Comp Neurol* 524: 3666–3673, 2016.

Yoganarasimha D, **Rao G**, **Knierim JJ**. Lateral entorhinal neurons are not spatially selective in cue-rich environments. *Hippocampus* 21: 1363–1374, 2011.

Yoganarasimha D, **Yu X**, **Knierim JJ**. Head direction cell representations maintain internal coherence during conflicting proximal and distal cue rotations: comparison with hippocampal place cells. *J Neurosci* 26: 622–631, 2006.

Zinyuk L, **Kubik S**, **Kaminsky Y**, **Fenton AA**, **Bures J**. Understanding hippocampal activity by using purposeful behavior: place navigation induces place cell discharge in both task-relevant and task-irrelevant spatial reference frames. *Proceedings of the National Academy of Sciences* 97: 3771–3776, 2000.

bioRxiv preprint doi: https://doi.org/10.1101/2020.10.17.343558; this version posted October 17, 2020. The copyright holder for this preprint (which was not certified by peer review) is the author/funder, who has granted bioRxiv a license to display the preprint in perpetuity. It is made available under aCC-BY-NC-ND 4.0 International license.

Tables

Statistical test	**Quantities compared**	**p**	**Z**	**Wilcoxon ranksum**	**χ2**	**# of samples in Prox CA1**	**# of samples in Dist CA1**
Wilcoxon rank sum	Mean firing rate	0.37	0.89	27079		156 neurons	180 neurons
Wilcoxon rank sum	Peak firing rate	0.34	0.95	27128		156 neurons	180 neurons
Wilcoxon rank sum	Spatial information score	0.15	-1.45	24997		156 neurons	180 neurons
Wilcoxon rank sum	Number of place fields/cell	0.28	1.07	19968		139 place cells	140 place cells
Wilcoxon rank sum	Field size	0.13	-1.52	30915		181 place fields	176 place fields
Wilcoxon rank sum	Fraction of area occupied by place fields	0.78	-0.28	19272		139 place cells	140 place cells
χ2	Fraction of place cells with 1 place field/cell	0.36			0.85	107 place cells with 1 field out of 139 place cells	115 place cells with 1 field out of 140 place cells

Table 1. Statistical comparison of properties of proximal and distal CA1 neurons in the first standard session of the day.

Mismatch angle	**Prox CA1**			**Int CA1**			**Dist CA1**		
	U	**Critical value of U for p < 0.001**	**n**	**U**	**Critical value of U for p < 0.001**	**n**	**U**	**Critical value of U for p < 0.001**	**n**
45°	20333.32	163.60	58	20298.83	170.54	49	20360.76	163.60	57
90°	19622.83	172.58	41	19918.09	172.58	41	19408.52	170.54	49
135°	20010.00	170.54	48	19098.39	172.58	41	18588.52	172.58	44
180°	17530.99	177.88	35	18459.68	184.05	27	16786.14	163.60	55

Table 2. Rao's spacing test statistics (Rao 1976; Russell and Levitin 1995) for single unit rotation data shown in Figure 4. All tests were significant with $p < 0.001$.

bioRxiv preprint doi: https://doi.org/10.1101/2020.10.17.343558; this version posted October 17, 2020. The copyright holder for this preprint (which was not certified by peer review) is the author/funder, who has granted bioRxiv a license to display the preprint in perpetuity. It is made available under aCC-BY-NC-ND 4.0 International license.

Mis ang	**Prox CA1**					**Int CA1**					**Dist CA1**				
	MVA	**MVL**	**p**	**z**	**n**	**MVA**	**MVL**	**p**	**z**	**n**	**MVA**	**MVL**	**p**	**z**	**n**
45°	-7°	0.83	$< 10^{-5}$	40.2	58	2°	0.82	$< 10^{-5}$	33.5	49	-5°	0.91	$< 10^{-5}$	46.9	57
90°	35°	0.41	0.0009	6.8	41	-13°	0.67	$< 10^{-5}$	18.3	41	-14°	0.56	$< 10^{-5}$	15.3	49
135°	16°	0.25	0.0486	3.0	48	-1°	0.22	0.1331	2.1	41	-45°	0.29	0.0268	3.6	44
180°	107°	0.39	0.0131	4.3	35	-80°	0.15	0.5674	0.6	27	-84°	0.15	0.3085	1.2	55

Table 3. Rayleigh test for uniformity for single unit rotation data shown in Figure 4. MVA and MVL denote mean vector angles and lengths, z denotes Rayleigh's z. Negative MVAs denote CW rotation in the direction of the global cues, while positive MVAs denote CCW rotation in the direction of the local cues.

Mismatch angle	Region	Number of points in cluster 1	Number of points in cluster 2
45°	Prox CA1	991	9
	Dist CA1	1	999
90°	Prox CA1	963	37
	Dist CA1	4	996
135°	Prox CA1	534	466
	Dist CA1	0	1000
180°	Prox CA1	995	5
	Dist CA1	2	998

Table 4. Number of points from proximal and distal CA1 assigned to clusters 1 and 2 by k-means clustering (k = 2). For ease of visualization, after running the k-means clustering algorithm, the cluster with higher number of points from proximal CA1 was named cluster 1, while the other cluster with higher number of points from distal CA1 was named cluster 2.

Figure Legends

Figure 1. CA1 circuitry and experimental paradigm. (A) Schematic showing anatomical connectivity of CA1 along its transverse axis. Bidirectional arrows indicate reciprocal connections between the two connected areas; unidirectional arrows indicate direction of information flow. (B) Recording sessions included two mismatch sessions interleaved between standard sessions. All but one rat encountered 2 standard sessions before manipulations began for a total of 6 sessions each day, while one rat encountered only one standard session before manipulations began for a total of 5 sessions each day. Standard sessions had local as well as global cues in the configuration the rats were trained on, while mismatch sessions had local cues rotated CCW and global cues rotated CW by equal amounts to get a net cue mismatch of 45°, 90°, 135°, or 180°. (C) Examples of tetrodes recording along the transverse axis

bioRxiv preprint doi: https://doi.org/10.1101/2020.10.17.343558; this version posted October 17, 2020. The copyright holder for this preprint (which was not certified by peer review) is the author/funder, who has granted bioRxiv a license to display the preprint in perpetuity. It is made available under aCC-BY-NC-ND 4.0 International license.

of CA1 from one rat. The drive canulae were linearly organized in ~ 3 rows oriented at 35° to the ML axis to target the entire extent of the transverse axis at the same septotemporal level.

Figure 2. Properties of putative pyramidal cells along the transverse axis of CA1. Mean firing rates, peak firing rates, spatial information scores, number of place fields per cell, place field sizes, and fraction of the track occupied by place fields in the proximal, intermediate, and distal CA1 during the first standard session of the day.

Figure 3. Single unit responses to cue manipulation. (A) Examples of units showing different types of responses to cue manipulations. Responses were categorized into 5 types: CW rotation in the direction of the global cues, CCW rotation in the direction of the local cues, ambiguous rotation, appear in MIS session and disappear in MIS session. Peak firing rates and spatial information scores are shown under each rate map. Asterisks mark statistically significant spatial information scores. (B) Proportion of different classes of responses in proximal, intermediate, and distal CA1 pooled across the 4 mismatch angles.

Figure 4. Distribution of single cell rotation angles in response to increasing mismatch angles. Angle of rotation of each rotating unit between STD and MIS sessions is represented by a dot around a circle. Mean vector computed from the rotation angles of all units for the given MIS angle is represented by a blue arrow in the center. Angles of rotations of cues between STD and MIS sessions are represented by dotted lines; local and global cue rotations are marked by the letters L and G. (B) Pie charts showing proportions of rotating units summed across all mismatch angles.

Figure 5. Population vector correlations. Population vector correlation matrices for STD1 vs STD2 sessions (STD sessions preceding and following MIS session) and STD1 vs MIS session show magnitude of correlation between population vectors for each 1° position bin on the track as a function of relative displacement between the two sessions being compared. STD1 vs STD2 matrices show a strong band of high correlation around 0° displacement (black line) for all mismatch angles and all subregions of CA1. Red and green lines show the expected displacement of high coherence band corresponding to local and global cue rotations in the different mismatch sessions, respectively. STD1 vs MIS matrices show different responses at different mismatch angles for different regions. While distal CA1 STD1 vs MIS matrices show a distinct band of high correlation following global cue rotation (green line) at all mismatch angles, proximal and intermediate CA1 STD1 vs MIS matrices show patchy distribution of high correlation at multiple mismatch angles. Polar plots below the population vector correlation matrices show mean of population vector correlations over all positions at each relative displacement (0°-359°). Magnitudes of positive mean correlations are shown in blue while magnitudes of negative mean correlations are shown in green. Black line in the center shows mean vectors computed from the polar plots. Notice the reduced peak correlations at higher mismatch angles for all regions compared to STD1 vs STD2 correlations and STD1 vs MIS correlations at 45°. Contrast the butterfly wings like structure of positive correlations for proximal CA1 at 90° and 135° with the larger peak following the global cues for distal CA1. The outermost circle in the polar plot corresponds to Pearson correlation coefficient of 1 with each concentric circle being spaced at 0.2.

bioRxiv preprint doi: https://doi.org/10.1101/2020.10.17.343558; this version posted October 17, 2020. The copyright holder for this preprint (which was not certified by peer review) is the author/funder, who has granted bioRxiv a license to display the preprint in perpetuity. It is made available under aCC-BY-NC-ND 4.0 International license.

Figure 6. Bootstrap analysis. Bootstrapped distributions were created for proximal and distal CA1 by resampling, with replacement, neurons in the two regions 1000 times. Number of samples in each iteration matched the number of neurons in the actual dataset. Peak vectors (x,y pairs), FWHM, and normalized bias were measured from the mean population vector correlations for all iterations. For each mismatch angle, PCA was run on this 4-dimensional space and the first two principal components were plotted to enable visualization of the bootstrapped distribution for proximal (red dots) and distal (blue dots) CA1. Notice tighter clustering of distal CA1 points compared to proximal CA1 points, which often form multiple clusters. k-means clustering (k = 2) was performed on the 4-dimensional data to classify the bootstrapped distributions into two clusters (black and cyan circles around the points). Notice how almost all of the distal CA1 points belong to one cluster while almost all of the proximal CA1 points belong to the other cluster for all mismatch angles other than 135° (see Table 4 for the numbers of points from each region belonging to each cluster). At 135°, proximal CA1 points almost evenly divide into the two clusters.

Figure 1

bioRxiv preprint doi: https://doi.org/10.1101/2020.10.17.343558; this version posted October 17, 2020. The copyright holder for this preprint (which was not certified by peer review) is the author/funder, who has granted bioRxiv a license to display the preprint in perpetuity. It is made available under aCC-BY-NC-ND 4.0 International license.

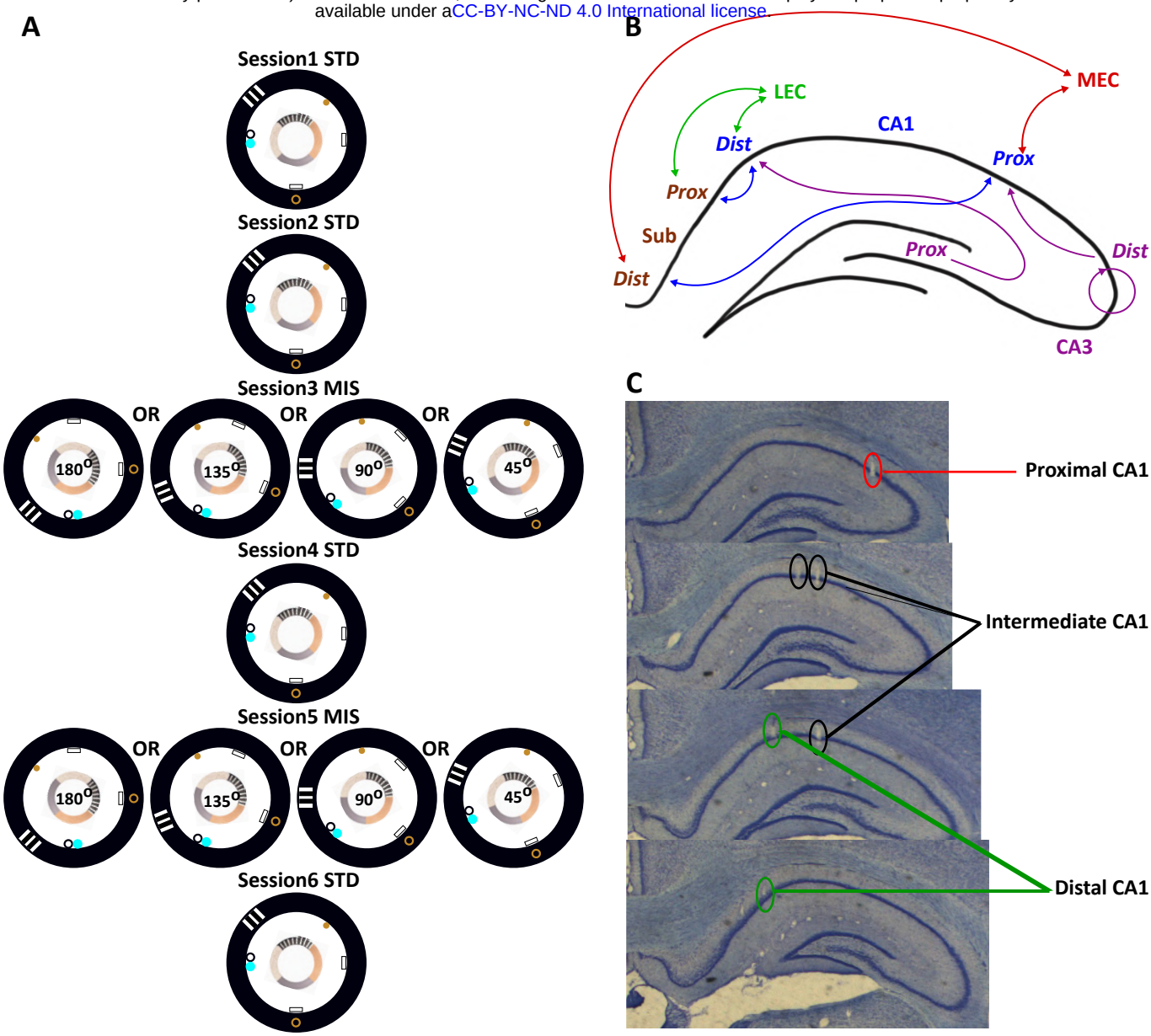

bioRxiv preprint doi: https://doi.org/10.1101/2020.10.17.343558; this version posted October 17, 2020. The copyright holder for this preprint (which was not certified by peer review) is the author/funder, who has granted bioRxiv a license to display the preprint in perpetuity. It is made available under aCC BY-NC-ND 4.0 International license.

Figure 2

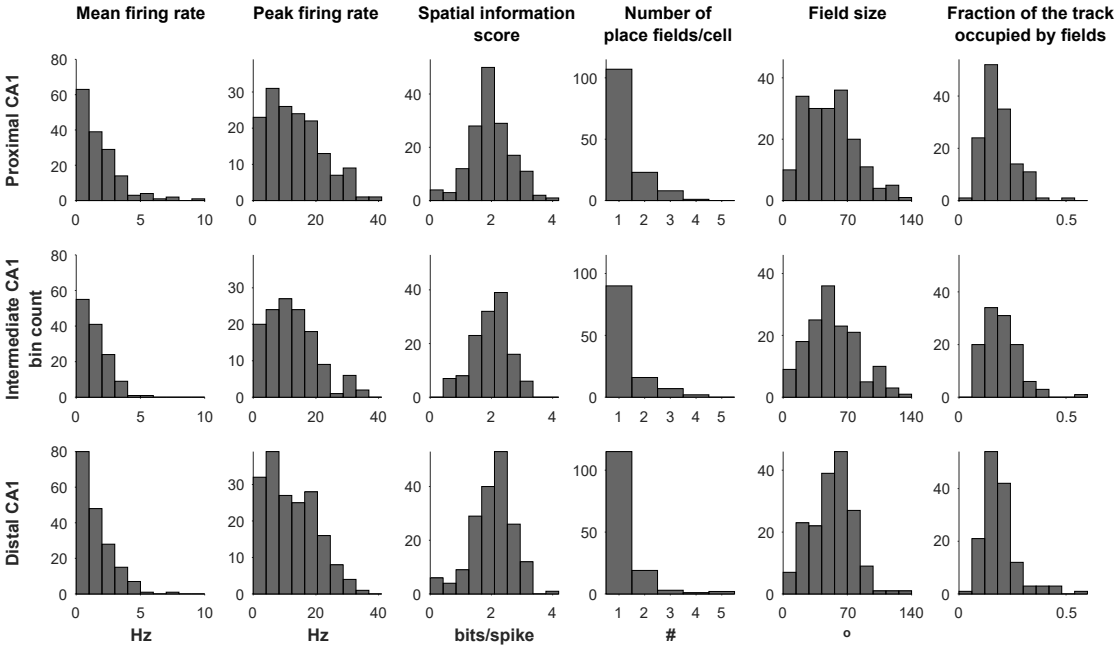

Figure 3

bioRxiv preprint doi: https://doi.org/10.1101/2020.10.17.343558; this version posted October 17, 2020. The copyright holder for this preprint (which was not certified by peer review) is the author/funder, who has granted bioRxiv a license to display the preprint in perpetuity. It is made available under aCC-BY-NC-ND 4.0 International license.

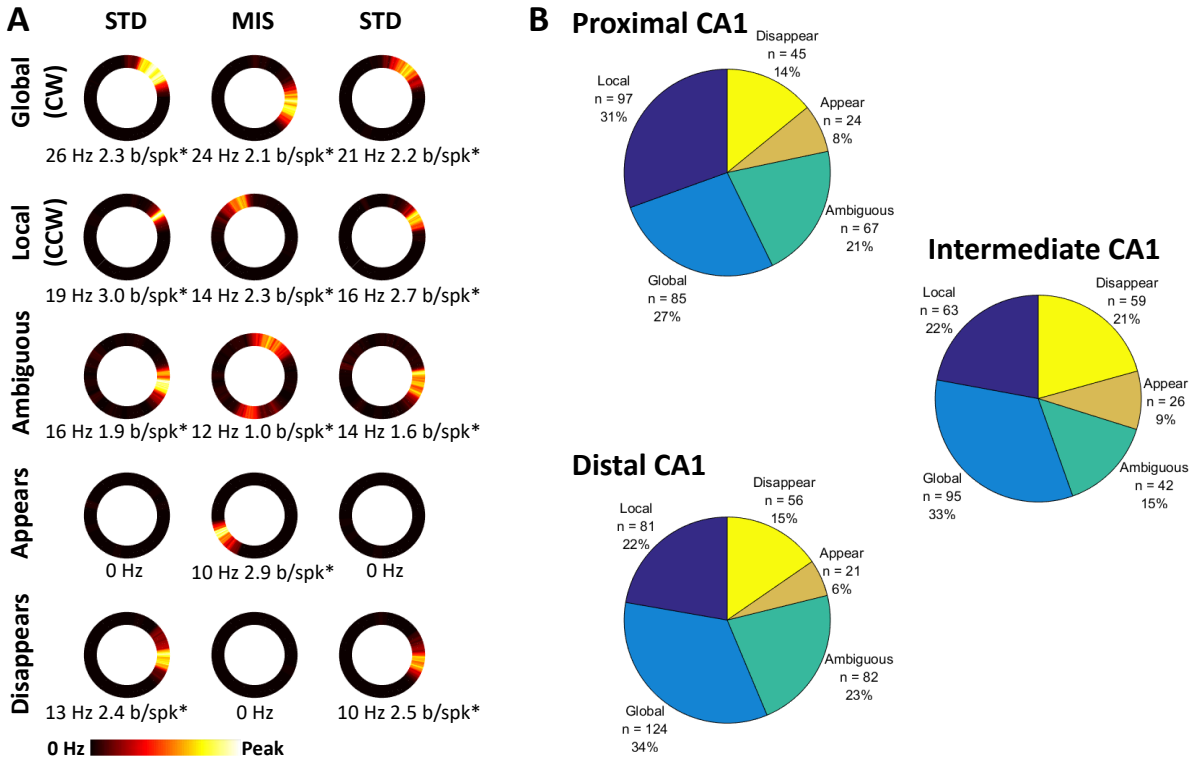

bioRxiv preprint doi: https://doi.org/10.1101/2020.10.17.343558; this version posted October 17, 2020. The copyright holder for this preprint (which was not certified by peer review) is the author/funder, who has granted bioRxiv a license to display the preprint in perpetuity. It is made available under aCC-BY-NC-ND 4.0 International license.

Figure 4

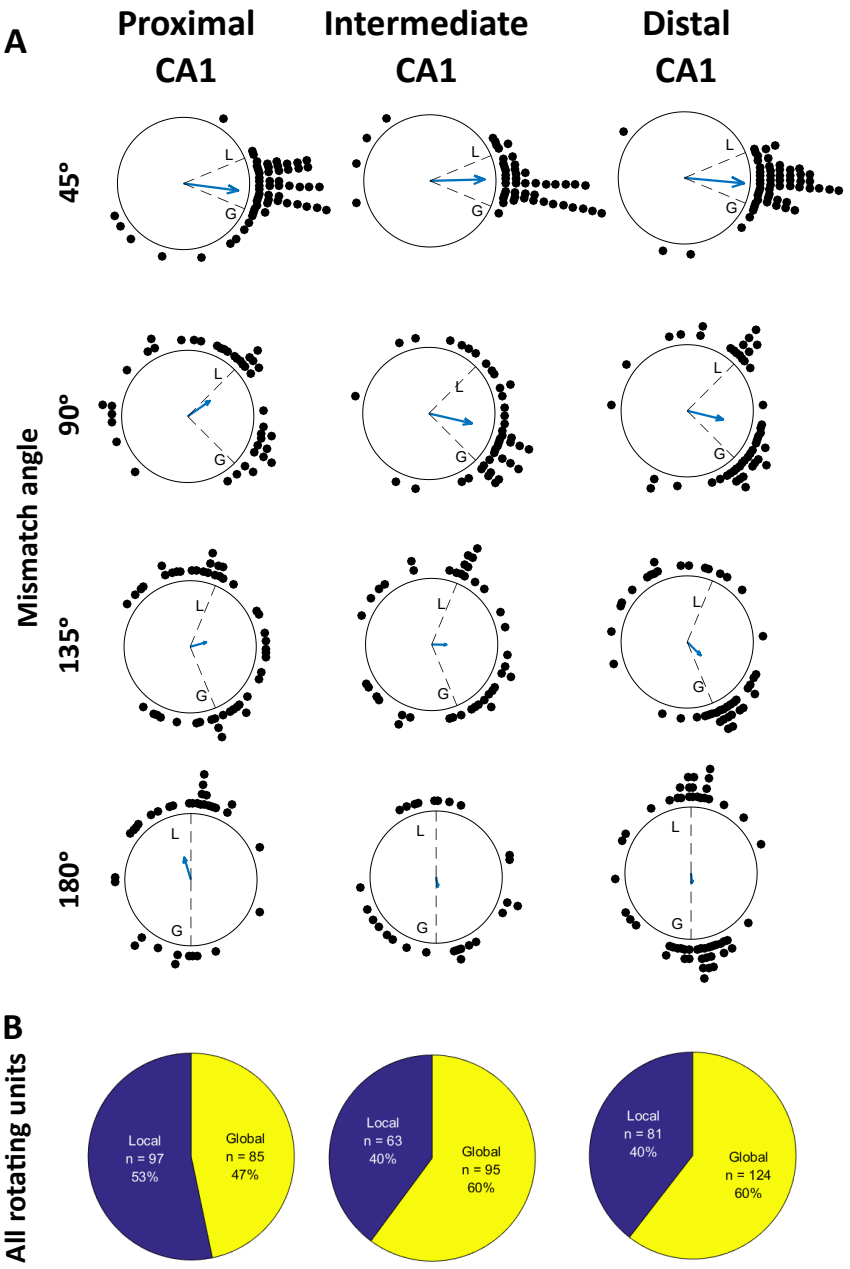

bioRxiv preprint doi: https://doi.org/10.1101/2020.10.17.343558; this version posted October 17, 2020. The copyright holder for this preprint (which was not certified by peer review) is the author/funder, who has granted bioRxiv a license to display the preprint in perpetuity. It is made available under aCC-BY-NC-ND 4.0 International license.

Figure 5

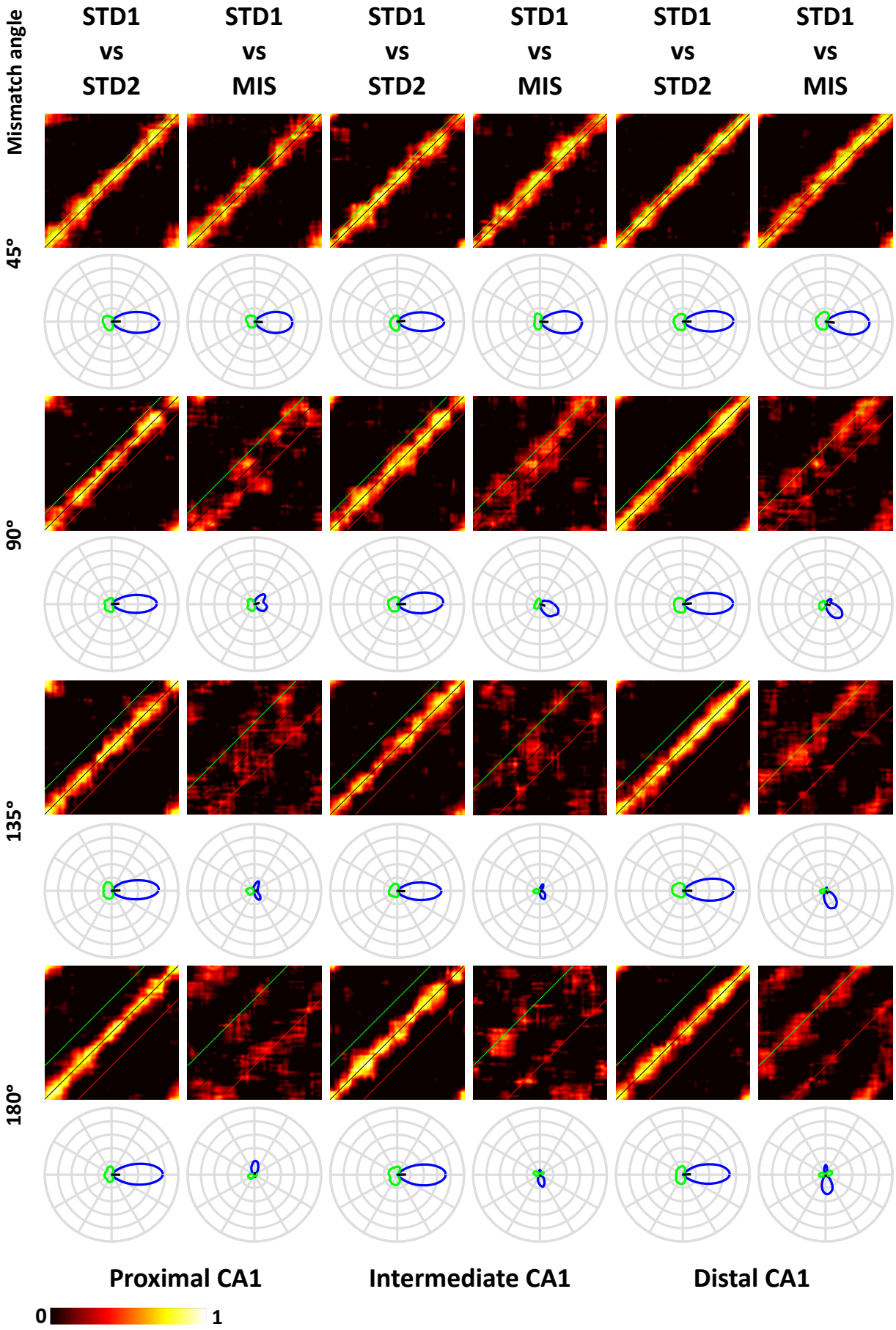

bioRxiv preprint doi: https://doi.org/10.1101/2020.10.17.343538, this version posted October 17, 2020. The copyright holder for this preprint (which was not certified by peer review) is the author/funder, who has granted bioRxiv a license to display the preprint in perpetuity. It is made available under aCC-BY-NC-ND 4.0 International license.
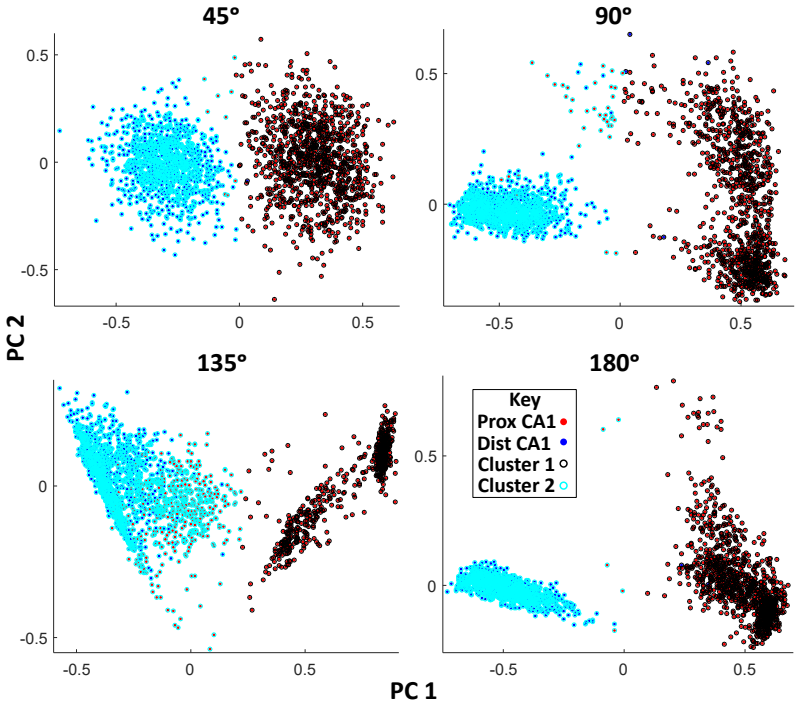
Figure 6